AM 9331 Revision 1 Word Count: 9413

Compositional effects on etching of fossil confined fission tracks in apatite

HONGYANG FU[1,2], FLORIAN TRILSCH[2,3], RAYMOND JONCKHEERE[2,*], and LOTHAR RATSCHBACHER[3]

[1] Key Laboratory of Tectonics and Petroleum Resources, Ministry of Education, China University of Geosciences, Wuhan, Hubei, 430074, PR China

[2] Endogene Geologie, TU Bergakademie Freiberg, 09599 Freiberg, Germany

[3] Institut für Keramik, Feuerfest- und Verbundwerkstoffe, TU Bergakademie Freiberg, 09599 Freiberg, Germany

ABSTRACT

Fission-track analysis is a thermochronologic method for dating rocks and reconstructing their low-temperature thermal histories. We investigate the influence of the apatite composition on the etching of fossil confined fission tracks, and its consequences for the fission-track method. We conducted step-etch experiments with 5.5 M HNO_3 at 21 °C on samples with etch pit diameters (*Dpar*) spanning most of the range for natural apatites (Panasqueira: 1.60 µm, Slyudyanka: 2.44 µm, Brazil: 3.92 µm, and Bamble: 4.60 µm) to determine their apatite etch rates v_R (the rate at which each lattice plane is displaced parallel to itself) as a function of crystallographic orientation (ϕ'). Our measurements revealed significant differences between the four samples. We fitted three-parameter functions, $v_R = a(Dpar)\,\phi'\,e^{b(Dpar)\phi'} + c$, describing v_R as a function of the angle to the apatite ***c***-axis for our hexagonal samples (excluding Bamble) and Durango apatite. The parameters *a* and *b* both exhibit a linear correlation with *Dpar*, whereas the constant *c* is small (~0.1 µm.min^{-1}) and its between-sample variation negligible at the resolution of our measurements. Bamble exhibits a different, bimodal relationship between v_R and ϕ', which we fitted with a sum of two sine functions. In all cases, including Bamble, there is a striking correlation between the angular frequencies of horizontal confined tracks and the magnitude of the apatite etch rate v_R perpendicular to the track axes. This shows that the sample of confined tracks selected for measurement and modeling is to a much greater degree determined by the etching properties of the apatite sample than by geometric or subjective biases. The track etch rate v_T is constant along most of the track length but varies from track to track. The mean v_T correlates with *Dpar*, so that tracks etch to their full lengths in a shorter time in faster etching apatites. The mean rate of length increase between etch steps, v_L, also correlates with *Dpar*. The length increments of individual tracks are however irregular. This points to an intermittent structure at the ends of the tracks.

Keywords: apatite, fission-track, confined track, track revelation, apatite etch rate, track etch rate

*Corresponding author: Raymond.Jonckheere@geo.tu-freiberg.de

1. INTRODUCTION

Fission-track analysis is a thermochronologic method for determining the ages of rocks and for reconstructing their thermal histories. It is based on counting and measuring etched trails of lattice damage within suitable minerals, left by the fragments of fissioned uranium nuclei. There are unanswered fundamental questions regarding how the tracks that are counted and measured after etching are related to the original damage trails. Geometric biases affecting confined track-length measurements are understood (Laslett et al. 1982, 1984; Galbraith et al. 1990; Galbraith 2002, 2005; Ketcham 2003, 2005), but biases related to the actual etching of confined tracks are less clear. The lengths of confined tracks in apatite are affected by the etching conditions, including etchant, concentration, duration, and temperature (Barbarand et al. 2003; Moreira et al. 2010; Ravenhurst et al. 2003; Sobel and Seward 2010; Tello et al. 2006; Figure 1 and references in Jonckheere et al. 2017). Ketcham (2003) found that geometric biases (Galbraith et al. 1990; Galbraith 2002) alone cannot account for the angular distributions of confined tracks and proposed that "under-etching bias" was also a factor. The inclusion of under-etched tracks and subjective biases affecting the selection of confined tracks for measurement by a particular analyst have been interpreted to account for the lack of inter-analyst agreement (Ketcham et al. 2015; Tamer et al. 2019; Tamer and Ketcham 2020; Ketcham and Tamer 2021).

The prevailing model describes track etching as the combined effect of the etch rate v_T of the damaged material along the track and the bulk etch rate v_B of the undamaged material in all other directions (Price and Walker 1962; Price and Fleischer 1971; Tagami and O'Sullivan 2005; Hurford 2019; Ketcham and Tamer 2021). Step-etch experiments showed that the lengths of individual confined tracks in apatite increase ~0 to >1 μm during 10-s etch-time increments following an initial 20 s etch (Jonckheere et al. 2017). This illustrates the importance of ascertaining the effective etch times of individual tracks for modeling the track-length distribution (Aslanian et al. 2021). Jonckheere et al. (2019, 2022) proposed a model explaining the geometries of etched tracks in which, instead of each individual point on a surface advancing at a rate v_B in all directions, crystallographic planes move as units during etching. Their etch rate v_R is a vector perpendicular to the plane equal in magnitude to its rate of displacement. This model implies that the shapes of etched tracks depend on their crystallographic orientation. Aslanian et al. (2021) measured v_R as a function of orientation for Durango apatite (etched with 5.5 M HNO_3 at 21 °C). The maximum width of a confined track (w) and the apatite etch rate perpendicular to the track (v_R) give an estimate of the true duration for which it was etched (effective etch time, t_E): $t_E = ½\ w/v_R$. The effective etch time is shorter than the immersion time by the time t_A, needed for the etchant to travel down the host track (v_T) and across to the confined track (v_R). This "access time" is different for each confined track (Laslett et al. 1984).

Donelick (1993) and Burtner et al. (1994) found a correlation between the etch rate (etch-pit size, *Dpar*) and the anion composition (F, Cl, OH) of different apatites; apatites with higher of Cl- or OH-contents have a greater *Dpar*. Thus, the apatite composition influences the effective etch times, widths, and lengths of the confined tracks selected for measurement and modeling. The following sections report step-etch experiments aimed at determining v_R for different apatites and relating them to a common reference. Our further aim is that this understanding should lead to improved etch protocols, tailored to individual apatites (Ravenhurst et al. 2003), as a step towards improved thermal histories.

2. Materials and Methods

We report step-etch experiments on four apatites with different chemical compositions and etch rates, as reflected in the sizes of the etched track openings parallel to the ***c***-axis (*Dpar*; Donelick 1993): Panasqueira (PQ; *Dpar* = 1.60 µm), Slyudyanka (SY; *Dpar* = 2.44 µm), Brazil (BZ; *Dpar* = 3.92 µm) and Bamble (BB; *Dpar* = 4.60). Prism sections of these apatites were mounted in resin, ground on SiC paper, polished with 6-, 3-, and 1-µm diamond suspensions, and fine-polished with 0.04-µm silica suspension until their surfaces appeared smooth under reflected light. We first etched the samples in a stirred 5.5 M HNO_3 solution at 21 °C (Carlson et al. 1999) for times in approximate inverse proportion to their *Dpar*, so as to start off with more or less similar tracks and a minimum track overlap after a subsequent etch step: 35 s for PQ, 20 s for SY, and 10 s for BZ and BB (Figure 1). Etching was stopped by consecutive immersion in two beakers with deionized water. We then rinsed the samples with ethanol and dried them in a curing cabinet at 35 °C. Following the first series of measurements, we etched the samples for a second time in 5.5 M HNO_3 at 21 °C for 15 s for the slow-etching (PQ and SY) and a 10 s for the fast-etching apatites (BZ and BB). For these conditions, the initial widths and the width increments are comparable to those for Durango apatite (DR) in Aslanian et al. (2021). Before the track measurements, we measured the surface etch pits parallel to the ***c***-axis (*Dpar*) in separate mounts of PQ, SY, BZ and BB etched in 5.5 M HNO_3 solution at 21 °C for 20s (Table 2).

We built a database consisting of the locations and images of suitable confined tracks in each sample using a motorized Zeiss AxioImager Z2m microscope and Autoscan software. We scanned the samples in transmitted light at 250× optical magnification (100× dry objective and 2.5× post-magnification) recording image stacks of six frames with 0.25 µm offset (height 1.25 µm). Confined tracks (TinT) with both tips in sharp focus plunge <5° and can be considered as horizontal and measured with negligible error. Horizontal tracks are also sandwiched between two prism planes parallel to the surface; thus, the measured track width reflects the actual width of the blade of knife-blade shaped tracks, not an apparent width (Gleadow 1981). We measured the same tracks after the first and second immersion in the etchant, except for some that had come to intersect the surface or became obscured by neighboring tracks. Depending on the case, we extracted the clearest image from a stack or compressed several into a single image, cut out a square frame centered on the confined track, and converted it to eight-bit greyscale. We imported these images into the CorelDraw graphics-suite software for measurement. We placed a circle tangent to facing sides of the track at its intersection with the host track to measure its width, and a second at some distance from the first to determine the track etch rate (Figure 1a-c). Tracks sub-orthogonal to the ***c***-axis ($\phi \gtrsim 80°$) develop a diamond-shaped etch figure, bounded by the fastest-etching faces, at their intersection with the host track (Figure 1d; Jonckheere et al. 2022). In this case, we measured the distances (d_1 and d_2) between opposing sides of the diamond shapes for calculating their effective etch times.

The apatite etch rates (v_R), track etch rates (v_T), and effective etch times (t_E) were calculated following Aslanian et al. (2021):

$$v_R\ (\mu\text{m/min}) = \frac{1}{2}\ \frac{\Delta r_0(\mu\text{m})}{\Delta t_I(\text{min})} \quad (1)$$

DOI: https://doi.org/10.2138/am-2024-9331. http://www.minsocam.org/

$$v_L\ (\mu\text{m/min}) = \frac{1}{2}\ \frac{\Delta l(\mu\text{m})}{\Delta t_I(\text{min})} \tag{2}$$

$$\theta = 2\arcsin\left(\frac{(r_0 - r_1)(\mu\text{m})}{2s_1(\mu\text{m})}\right) \tag{3a}$$

$$v_T\ (\mu\text{m/min}) = \frac{1}{2}\ \frac{v_R(\mu\text{m})}{\sin(\theta/2)} \tag{3b}$$

$$t_E\ (s) = 30\ \frac{r_0(\mu\text{m})}{v_R(\mu\text{m/min})} \qquad (\phi \lesssim 80°) \tag{4a}$$

$$t_E\ (s) = 15\ \frac{(d_1 + d_2)(\mu\text{m})}{v_{R,MAX}(\mu\text{m/min})} \quad (\phi \gtrsim 80°) \tag{4b}$$

Δr_0 is the track width increase at its intersection with the host track (r_0) due to the second immersion; Δt_I the time increment from the first to the second etch; s_1 is the distance between the centers of both circles (r_0 and r_1; Figures 1 and 2); θ the angle between facing straight sides of the confined track; ϕ its angle to the ***c***-axis; d_1, d_2 the distances between opposite sides of the diamond shapes. (Figure 1d). Table 1 gives an overview of the symbols used.

3. Results and Discussion

This section covers our length (3.1) and width measurements (3.2), including the calculation of v_R and its correlation with *Dpar*, the calculation of the effective etch times t_E (3.3), the relationship between v_R and angle to the ***c***-axis ($\phi' = 90 - \phi$) (3.4.), the calculation of the track etch rates v_T and the rates of length increase v_L, and their relationships with *Dpar* (3.5.). Tables 2 to 5 summarize the main statistics.

3.1. Track Lengths

Table 2 summarizes the track-length data. Even considering the non-standard immersion times, PQ and SY, with mean lengths <14 µm and standard deviations >1.5 µm, plot squarely in the field of basement apatites (Gleadow et al. 1986; Figure 3). BB and DR (Durango data from Aslanian et al. 2021), with mean lengths >14 µm and standard deviations of ~1 µm, are close to the volcanic apatites. BB plots at first between the basement and volcanic fields but in view of the short first etch (10 s), it belongs in the latter, wherein it plots after another 10 s. Although BZ contains fossil tracks, it plots at the edge of the induced-track field after 10 s immersion and in it after 20 s, with a greater mean length (>15 µm) and a lower standard deviation (<1 µm) than the average for induced tracks. Supplement Figure S1 shows the track lengths plotted against angle to the ***c***-axis. Figure S2 plots the length increments Δl between the first and second etch against angle to the ***c***-axis and the corresponding distributions. The increments differ from track to track with no clear dependence on the track orientation. Δl-values range from ~0 to ≳2 µm, which is well within the resolution of our measurements based on image pairs (Figure 1). The irregular increments suggest that latent tracks are discontinuous towards their ends (Paul and Fitzgerald 1992; Li et al. 2011; Jonckheere et al.

2017). The average increment is isotropic but differs from sample to sample with a minimum Δl_M < 0.5 µm for PQ (Δt_I = 15 s) and maximum Δl_M > 1.0 µm for BZ (Δt_I = 10 s). The apparent isotropic length increase and the correlation with *Dpar* support the notion that tracks become terminated by the slowest-etching apatite faces, i.e., the prism and basal face (Jonckheere et al. 2019). Figure 4 plots the individual track lengths after the second etch against those after the first. Geometric mean regression lines fitted to the data have slopes S_L from 0.95 to 1.05 and correlation coefficients from 0.87 to 0.99. However, constrained regression lines, with unit slope (S_L = 1), also provide a good fit (Table 3). This suggests that the length increments are independent of the initial lengths, in contrast with earlier findings for Durango apatite, indicating that the lengths of shorter fossil tracks increased less than those of longer ones for an etch time increment from 20 to 60 seconds (Jonckheere et al. 2017).

Ellipses fitted to the lengths (l) and orientations (ϕ) measured after the first immersion indicate that the fossil track lengths are less anisotropic than those of induced tracks annealed to the same mean ***c***-axis value. The ***c***-axis and ***a***-axis intercepts plot between the isotropic line (1:1; l_A = l_C) and the trend for induced tracks annealed to different degrees under laboratory conditions (Figure 5; RD: l_A = 1.632 l_C - 10.879). Donelick et al. (1999) report abundant data showing that this is a common observation for fossil fission tracks in geologic samples. They remark that its cause is uncertain, suspecting: (1) inaccurate identification of the ***c***-axis, or (2) an unspecified effect related to fitting ellipses to fossil track populations, comprising tracks with different thermal histories. In first instance, the ***c***-axis and ***a***-axis intercepts of an ellipse fitted to the sum of two or more populations on the RD line are the weighted means of those of its components, and also plot on the RD line. Possible causes for deviations are: (1) the component populations have different angular distributions, so that their relative weight varies with the angle to the ***c***-axis; (2) length bias (Laslett et al. 1984; Galbraith et al. 1990) causes to overestimate the weight of populations consisting of longer tracks; this effect is somewhat greater for the shorter high-angle tracks than for the longer low-angle tracks.

In the case of our samples, neither cause could account for more than a small departure from the RD-trend. It is also improbable that the ***c***-axis orientations have been misidentified in our prism sections. In addition to the usual criteria (habit, inclusions, track openings), the ***c***-axis azimuth orientation can be inferred from the outline of each track (Figure 1; Aslanian et al. 2021; Jonckheere et al. 2022). After the second etch, all samples, except PQ, plot near to the RD-trend. The mean length has increased by a different amount in different samples, but by the same amount in all directions in each sample, including along the ***a***- and ***c***-axes (Figure S2), i.e., parallel to the 1:1-line in Figure 5. We suggest that this is an indication that geologic annealing results in an anisotropic shortening of the tracks along the RD-line, like induced tracks annealed in the lab, but also in a lowering of the track etch rate v_T. The latter, we expect, depends on the composition of the apatite as well as on the thermal histories of individual samples or even those of individual tracks (section 3.5).

3.2. Apatite Etch Rates

Plots of the confined track widths (r_0) against their ***c***-axis angles (ϕ) for consecutive immersions reveal a distinct angular dependence (Figure S3). The tracks in PQ, SY, and BZ have maximum widths of ~2.5, ~2, and ~1 µm at 60-75° to the ***c***-axis after the first immersion. In contrast, the track widths in BB have a bimodal distribution with ~1 µm maxima at 15-30° and 60-75° to the ***c***-axis. We calculated the apatite etch rates v_R from the width increase Δr_0 of individual tracks for our four samples (equation 1). PQ, SY, BZ, and BB all have v_R-maxima of ~3, ~4 and >5 µm.min^{-1} at 15-30° to the ***c***-axis, decreasing to <1 µm.min^{-1} (BZ, BB) or <0.5 µm.min^{-1} (PQ, SY) parallel and perpendicular to the ***c***-axis. The Bamble apatite has a second local v_R-maximum of >4 µm.min^{-1} at 40-50° to ***c***, owing to its different crystal structure (Figure 6a and b). Although we have no crystallographic data for our samples, Bamble is known to have a patchy hexagonal and monoclinic structure (Taborszky, 1972), which may explain its broader maxima compared to the other apatites. We constructed polar plots of the radial etch rate v_R by mirroring the v_R interval between 0 and 90° about the ***c***-axis and about an axis perpendicular to it (Figure 6c).

We fitted empirical equations to the angular v_R-distributions of our four apatites and the published Durango data of Aslanian et al. (2021) (Table 4). For the hexagonal apatites, we used an equation of the form:

$$v_R = a\phi' \, e^{b\phi'} + c \qquad (5)$$

The constant c is not correlated with *Dpar* and has almost no influence on the fit; $c = v_R(0)$ is the etch rate parallel to the ***c***-axis, where v_R has a cusp-shaped minimum and its angular variation is greatest, so that it is difficult to estimate c. As v_R cannot be 0, we set $c = 0.1$. a and b exhibit a linear dependence on *Dpar*; their common dependence on *Dpar* means that a and b are not independent of each other (Figure 7). Despite its small range, the variation of b in tandem with a is significant in the angular interval $0° \leqslant \phi' \leqslant 90°$.

$$a = 0.141(8)\, Dpar + 0.09(2) \qquad r = 0.99 \qquad (6)$$

$$b = -0.0017(5)\, Dpar - 0.047(1) \qquad r = 0.93 \qquad (7)$$

which gives:

$$v_R = (0.141\, Dpar + 0.09)\phi' \, e^{(-0.0017\, Dpar - 0.047)\phi'} + 0.1 \qquad (8)$$

Equation (8) highlights that, for hexagonal apatites, v_R correlates with *Dpar* for all ***c***-axis angles. We fitted a bimodal trigonometric equation to the v_R *vs.* ϕ' data for the non-hexagonal Bamble apatite:

$$v_R = 0.88(11)\, sin(5.56(12)\phi') + 3.69(34)\, sin(2.08(3)\phi') + 0.76(28) \qquad (9)$$

3.3. Effective Etch Times

Figure S4 plots the effective etch times of the confined tracks against their ***c***-axis angles. The boomerang shapes reflect the fact that tracks sub-orthogonal to the v_R-minima parallel and perpendicular to the ***c***-axis require longer etching than those at intermediate angles to become wide enough to be selected for measurement (Gleadow 1981). Some t_E-values for thin tracks at low and at high angles to the ***c***-axis exceed the immersion time. This could indicate that t_E-calculations have limited precision, although, since the difference is <2 s, it could in part be due to a lingering residue of the etchant in the thinnest tracks at the moment the samples are immersed in water to halt the etching process. The t_E-distributions are right-skewed, with geometric means just over ½ t_I and standard deviations just under ⅕ t_I (Figure S4). The mean track lengths and track densities, defining the fundamental geometric relationships, e.g., the average separation, between host tracks and confined tracks appear to have no significant influence on the effective etch times of the confined track sample (Tables 2 and 5). For example, the surface track density of BZ is more than ~17 times greater than that of BB but their mean effective etch times after their initial 10 s immersion in the etchant differ by less than ~10%.

Jonckheere et al. (2017; their Figure 1) proposed "*etchant strength*" as the product of the etchant concentration and immersion time to measure their combined influence on the etched lengths of confined tracks in apatite. Although it is not evident that etchant strength alone determines the track length, it did harmonize the step-etch data obtained with different protocols. We define "*etch action*" ($t'_I = Dpar \times t_I$) as the product of the apatite etch rate and immersion time to compare the results of one etchant (5.5 M HNO_3) across different apatites. Although the apatite etch rate is anisotropic, the previous result implies that *Dpar* (Donelick 1993) characterizes the overall apatite etch rate. Figure 8a shows a line of equal etch action: $Dpar \times t_I = 50$ µm.s, and the positions of our samples relative to that line. Most samples have a reasonable, although not a perfect, fit. The t_I for BZ is short because a longer immersion would have caused excessive track overlap ($\rho_S > 10^7$ cm^{-2}). In the same manner, we define the "*effective etch action*" ($t'_E = Dpar \times t_E$) of individual tracks with calculated individual effective etch times. Figure 8a and 8b show the means and the standard deviations of the effective etch time distributions plotted against *Dpar*. The means plot close to the line $Dpar \times t_{EM} = 25$ µm.s and the standard deviations plot close to the line $Dpar \times \sigma_{tE} = 10$ µm.s. Thus, the effective etch time distributions scale with the immersion times, with $t_{EM} \approx ½\ t_I$. The fact that the standard deviation also scales with t_I implies that it reflects actual t_E-variation and not just random measurement errors.

3.4. Angular Distributions

Figure S3a-d plots the widths of the confined tracks against their ***c***-axis angles. The dotted lines (1) represent the maximum track width for each orientation ($v_R(\phi') \times t_I$; t_I = 35 s (PQ), 20 s (SY), 10 s (BZ), and 10 s (BB)). The solid line (2) is an estimate of the actual maximum widths, allowing for the access time t_A that the etchant needs to reach the confined track before it can begin to etch it, i.e., for travelling down the host track and across to the confined track (Laslett et al. 1984; Rebetez et al. 1988; Ketcham and Tamer 2021). We set t_A = 6 s (PQ), 3 s (SY), 2 s (BZ), and 2 s (BB) based on the effective etch time calculations (Figure S4). The long-dashed line (3) represents a minimum width for tracks to be distinguishable and considered to be measurable under the microscope. We assumed a value of ~0.2 µm based on the minimum measured widths of the tracks in our samples. The short-dashed line (4) is the minimum width at the host track intersection at the moment that the etchant reaches the track tips; the calculated value for confined tracks etched from the middle towards both ends is:

$$w_{MIN}(\phi)(\mu\text{m}) = \left(\frac{v_R(\mu\text{m/min})}{v_T(\mu\text{m/min})}\right) l(\mu\text{m}) \qquad (10)$$

The difference $\Delta w(\phi)$ between (2) and max(3,4) reflects the range of track widths for a given orientation. Figure S3e-h shows $\Delta w(\phi)$ superimposed on the distributions of the angular frequencies of the measured confined tracks F(ϕ). The good fit and the striking contrast between the hexagonal apatites (PQ, SY, BZ) and the distinctive distributions for the Bamble apatite (BB; Donelick et al. 1999) are convincing proof that the angular frequencies are controlled by the anisotropic rate of widening of the confined tracks rather than the host track cross-section (Galbraith et al. 1990; Donelick et al. 1999; Galbraith 2002; Ketcham 2003). This also supports the notion that track width is the main criterion for confined track selection, although it is modified by factors depending on width and length. For instance, longer tracks attain a greater width before being etched to their ends than shorter tracks with the same orientation (equation 12). However, their impact on the angular distributions of the confined tracks is almost negligible due to the limited annealing of our samples.

3.5. Track Etch Rates

Figure S5 shows that the distributions of v_T are right-skewed; this could in part be related to its calculation, as random errors on the small angle θ in the denominator produce greater positive than negative deviations from the true v_T-value (equation 3). In this case, the geometric means provide more robust central estimates; these are 103 (PQ) and 95 μm.min^{-1} (SY) for the basement apatites and 197 (BZ) and 192 μm.min^{-1} (BB) for apatites with volcano-type length distributions (Gleadow et al. 1986). There is a significant positive correlation between the mean v_T and *Dpar* (r = 0.93; Figure 9a). A geometric mean regression line has the equation: v_T (μm.min^{-1}) = 9.2 (μm.min^{-1}) + 43.1 (min^{-1}) *Dpar*. However, a regression line anchored at the origin provides an equally good fit: v_T (μm.min^{-1}) = 46.3 (min^{-1}) *Dpar*. There is also a correlation between the standard deviations of the v_T distributions and *Dpar* (r = 0.67; Figure 9a). This lends support to the interpretation that the within-sample ranges of v_T-values are not just an artefact of their measurement and calculation. Here too, an unconstrained geometric mean regression line, σ_{VT} (μm.min^{-1}) = 4.6 (μm.min^{-1}) + 17.6 (min^{-1}) *Dpar*, and a regression line through the origin, σ_{VT} (μm.min^{-1}) = 23.2 (min^{-1}) *Dpar*, provide an almost equally good fit.

A causal connection implies that v_T, while tens of times greater than v_R, is nevertheless under compositional control. The track etch-rate measurements in apatite therefore reveal a complicated picture: (1) the straight edges of all confined tracks show that v_T is constant over most of the track length (Figures 1 and 2); (2) in contrast, v_T varies from track to track, with no clear dependence on orientation, giving rise to broad v_T-distributions with high standard deviations (Figure S5); (3) the differences between volcanic and basement apatites suggests an effect of time or temperature, such as seasoning (Bull and Durrani 1975), ageing (Gleadow et al. 1983), or thermal annealing (Fleischer et al. 1965). Price et al. (1973) concluded with respect to the track etch rates in silicate minerals that a "*gradual rearrangement of the damage at ambient temperature makes the properties of fresh tracks and of ancient tracks different*". All in all, this presents a quite different image of the track etch rate from the traditional concept, i.e., as a process controlled by chemical reaction rates rather than by physical factors related to track formation, such as along-track damage densities (Jonckheere 2003) or latent-track diameters (Li et al. 2012). The v_T-variation within a sample could then be a consequence of the individual histories of the tracks. On reflection, it is indeed not at all evident that the geologic histories of individual fission tracks lead to shortening of their etchable lengths without affecting the chemical properties of the remaining cores. If this result is confirmed, then the v_T-signatures of natural apatites could hold information about their geologic histories. For example, BB and BZ have similar v_T-distribution whereas those of SY and PQ, which are offset to lower values consistent with their lower *Dpar*, also present different characteristic shapes.

The v_L-distributions are right skewed (Figure S6): a small fraction of the tracks increases in length at twice to several times the average rate while the remainder increases at lower and more uniform rates. The means and standard deviations correlate with *Dpar* (Figure 9b). A geometric mean regression line to the v_L data is given by: v_L (μm.min^{-1}) = -0.39 (μm.min^{-1}) + 0.78 (min^{-1}) *Dpar* (r = 0.99); one anchored at the origin is also a good fit: v_L (μm.min^{-1}) = 0.65 (min^{-1}) *Dpar* (r = 0.99). Given that v_L is almost two orders of magnitude lower than v_T, this suggests that the length increase following the first immersion ($t'_I = t_I \times Dpar \approx 50$) is due to a chemical process controlled by the apatite compositions, with little influence of the properties or histories of the latent tracks, except perhaps to explain the differences between individual tracks. Through its measured width and orientation, each individual confined track is characterized by its effective etch time t_E after the first immersion (section 3.3). This allows us to track the mean length increase and length distribution between the first and second immersion as a function of the effective etch action (Figure 10a). Length estimates at regular intervals are obtained through linear interpolation between the measurements after the first and second immersion. The slopes of regression lines fitted to the data fall within a narrow range (1.11-1.13 min^{-1} for PQ and SY and 1.34-1.56 min^{-1} for BZ and BB; Table 3). Given the nature of the calculation, the difference needs not to be significant. In that case, past the limit of ca. 20 μm.s, the mean lengths of all our apatites have a common dependence on the effective etch action (1.29 min^{-1}).

In one respect, this is a trivial result: if the apatite etch rate remains constant during the immersion of a sample (Sobel and Seward 2010), then it is interchangeable with the immersion time. It follows that samples on a line of equal etch action (Figure 8a) are etched to the same degree and the tracks present similar widths and shapes. A careful scientist, selecting confined tracks based on their etched appearance, can then expect to measure track lengths and widths that are comparable between samples of different composition (sections 3.4 and 3.5). On the other hand, this means that apatites with different compositions are to different degrees under- or over-etched when using etching protocols with fixed immersion times. Figure 10b shows the data for step-etched fossil tracks in Durango apatite (Aslanian et al. 2021); the slope (1.64 min^{-1}) of a geometric mean regression line is somewhat steeper than the average for our samples but not inconsistent with it. Figure 10b also plots the mean lengths of unannealed induced tracks in a large set of apatites against the mean effective etch action, calculated from their *Dpar* and an assumed mean effective etch time of 11.5 s, which is our average for a 20 s immersion in 5.5 M HNO_3 at 21 °C (data from Carlson et al. 1999; Barbarand et al. 2003). The geometric mean regression line is given by: l_M (μm) = 15.64 μm + 1.38 (min^{-1}) × t'_E (μm.min), with correlation coefficient r = 0.89, in almost perfect agreement with equation (1) of Carlson et al. (1999). The slope of the regression line (1.38 min^{-1}) is also within the range of those of our samples (Table 3). The most economical interpretation is that the mean lengths of unetched induced tracks in all investigated apatites is 15.64 μm, regardless of their chemical composition, and that the measured differences among mean lengths are a consequence of bulk etching at different rates (Carlson et al. 1999). Our data show that the latter also applies to samples annealed in the geologic environment.

4. Implications

A simple empirical equation fitted to step-etch data describes the apatite etch rate v_R as a function of angle to the ***c***-axis (ϕ): $v_R = a\,\phi'\,e^{b\phi'} + c$. This equation applies to hexagonal apatites etched in 5.5M HNO_3 at 21 °C. The fitted constants, *a* and *b*, depend on a parameter related to the composition of the apatite (*Dpar*). This makes it possible, for each confined track in each apatite, to calculate the true duration for which it has been etched from its width at its intersection with the host track and *Dpar*, eliminating the need to determine the etch rates of each different sample or grain. This is the first empirical criterion for distinguishing well-etched from over- or under-etched tracks, and thus for limiting one source of spurious variation in Tt-modelling (Trilsch et al., in review). Our equation does not extend to non-hexagonal apatites, which exhibit a different dependence of v_R on ϕ.

The maximum attainable width of a confined track is proportional to the etch rate perpendicular to it, whereas its threshold (minimum) width is independent of its orientation. This accounts for the close correlation between the confined track widths and their angular frequencies. The implication is that we must consider etching-related biases as well as geometrical biases. In principle, we can formulate a length- and-orientation-bias model for each apatite-etchant combination for which the etch rate v_R is known as a function of orientation. As long as v_R scales with *Dpar*, this model should fit different apatite compositions for a given etchant. All a priori bias models must however be approximate because they ignore other etching-related factors, such as effective etch time t_E, track etch rate v_T, and the rate of length increase v_L. Measuring these characteristics along with the track lengths and orientations after the confined tracks have been selected instead helps to define the selection bias for each given sample. It is evident that understanding the relationship between a confined track sample and the track population is a condition for meaningful Tt-modelling (Galbraith, 2005).

Our data provide the first indication of a correlation between the track etch rate v_T and the apatite composition. The full implications are not clear, although such a correlation appears to favour an amorphous track core over a depleted core, and a thermal-spike track formation mechanism over a pure ion-explosion-spike mechanism. It suggests that the track etch rate is under chemical control and thus less dependent on, or independent of, the variation of the calculated lattice damage along the tracks. The v_T-variation from track to track could be due to the different masses, charges and energies of the track forming particles, but the significant differences between samples, over and above those caused by their apatite etch rates, suggest that v_T might bear an imprint of their thermal histories.

In all our samples, the mean confined track lengths increase at a constant rate v_L between the first and second measurement; v_L is similar to the apatite etch rate, which implies that the tracks were etched to their ends after their first immersion for a time $t_I \approx 50/Dpar$, however short it was, even as little as 10 seconds for fast etching apatites. The mean length increase Δl between the first and second measurement is then due to "bulk etching". The lengths of shorter tracks in a sample increase as much on average as those of the longer tracks. In first approximation, this implies that after the first immersion all the selected tracks in all our samples have reached something approaching their intrinsic length, which on continued etching increases in a predictable manner at an average rate proportional to *Dpar*. The Δl-distributions are nonetheless right-skewed (average skewness = 1.7) due a small number of tracks with much longer than average length increments. The negative correlation between Δl and t_E (mean r = -0.23) shows that these tracks began to etch last and were just short of bulk etching at the end of the first immersion. There are however too few in number to have an effect on the mean rate of length increase. The important implication is that, as of the end of the first immersion, the length distribution of the selected confined tracks in all our samples is a reflection of their formation and geological histories, not of their etching histories.

ACKNOWLEDGMENTS AND FUNDING

We are indebted to R. Donelick and R. Ketcham for reviewing our manuscript and for their helpful comments, and to D. Harlov for efficient editorial handling. Research funded by the Innovation Team Project of Natural Science Foundation of Hubei Province (Grant Number: 2021CFA031), the National Natural Science Foundation of China (Grant Number: 42372181) and the German Research Council (DFG projects JO 358/4 and Ra 442/42).

References Cited

Aslanian, C., Jonckheere, R., Wauschkuhn, B., and Ratschbacher, L. (2021) A quantitative description of fission-track etching in apatite. American Mineralogist, 106(4), 518-526.

Barbarand, J., Carter, A., Wood, I., and Hurford, T. (2003) Compositional and structural control of fission-track annealing in apatite. Chemical Geology, 198(1-2), 107-137.

Bull, R., and Durrani, S. (1975) Annealing and etching studies of fossil and fresh tracks in lunar and analogous crystals. In: Lunar Science Conference, 6th, Houston, Tex., March 17-21, 1975, Proceedings. Volume 3.(A78-46741 21-91) New York, Pergamon Press, Inc., 1975, p. 3619-3637. Research supported by the Science Research Council., 6, p. 3619-3637.

Burtner, R.L., Nigrini, A., and Donelick, R.A. (1994) Thermochronology of Lower Cretaceous source rocks in the Idaho-Wyoming thrust belt. AAPG bulletin, 78(10), 1613-1636.

Carlson, W.D., Donelick, R.A., and Ketcham, R.A. (1999) Variability of apatite fission-track annealing kinetics: I. Experimental results. American Mineralogist, 84(9), 1213-1223.

Donelick, R.A. (1993) A method of fission track analysis utilizing bulk chemical etching of apatite. U.S. Patent Number 5,267,274

Donelick, R.A., Ketcham, R.A., and Carlson, W.D. (1999) Variability of apatite fission-track annealing kinetics: II. Crystallographic orientation effects. American Mineralogist, 84(9), 1224-1234.

Fleischer, R., Price, P., and Walker, R. (1965) Ion explosion spike mechanism for formation of charged-particle tracks in solids. Journal of applied Physics, 36(11), 3645-3652.

Fleischer, R., Price, P., and Woods, R. (1969) Nuclear-particle-track identification in inorganic solids. Physical Review, 188(2), 563.

Galbraith, R., Laslett, G., Green, P., and Duddy, I. (1990) Apatite fission track analysis: geological thermal history analysis based on a three-dimensional random process of linear radiation damage. Philosophical Transactions of the Royal Society of London. Series A: Physical and Engineering Sciences, 332(1627), 419-438.

Galbraith, R.F. (2002) Some remarks on fission-track observational biases and crystallographic orientation effects. American Mineralogist, 87(7), 991-995.

-. (2005) Statistics for fission track analysis. CRC Press.

Gleadow, A. (1981) Fission-track dating methods: what are the real alternatives? Nuclear Tracks, 5(1-2), 3-14.

Gleadow, A., Duddy, IR, and Lovering, J. (1983) Fission track analysis: a new tool for the evaluation of thermal histories and hydrocarbon potential. The APPEA Journal, 23(1), 93-102.

Gleadow, A.J., Duddy, I., Green, P.F., and Lovering, J. (1986) Confined fission track lengths in apatite: a diagnostic tool for thermal history analysis. Contributions to Mineralogy and Petrology, 94, 405-415.

Green, P., Duddy, I., Gleadow, A., Tingate, P., and Laslett, G. (1986) Thermal annealing of fission tracks in apatite: 1. A qualitative description. Chemical Geology: Isotope Geoscience Section, 59, 237-253.

Hurford, A.J. (2019) An historical perspective on fission-track thermochronology. In: M.G. Malusà and P.G. Fitzgerald, Eds., Fission-Track Thermochronology and its Application to Geology, Geography and Environment, 3-23.

Jonckheere, R. (2003) On the densities of etchable fission tracks in a mineral and co-irradiated external detector with reference to fission-track dating of minerals. Chemical Geology, 200(1-2), 41-58.

Jonckheere, R., Aslanian, C., Wauschkuhn, B., and Ratschbacher, L. (2022) Fission-track etching in apatite: A model and some implications. American Mineralogist: Journal of Earth and Planetary Materials, 107(6), 1190-1200.

Jonckheere, R., Tamer, M.T., Wauschkuhn, B., Wauschkuhn, F., and Ratschbacher, L. (2017) Single-track length measurements of step-etched fission tracks in Durango apatite:"Vorsprung durch Technik". American Mineralogist, 102(5), 987-996.

Jonckheere, R., Wauschkuhn, B., and Ratschbacher, L. (2019) On growth and form of etched fission tracks in apatite: A kinetic approach. American Mineralogist: Journal of Earth and Planetary Materials, 104(4), 569-579.

Kelly, W., and GA, W. (1977) Paleothermometry by combined application of fluid inclusion and fission track methods. N.Jb. Min. Mh., Jg., 1-15.

Ketcham, R.A. (2003) Observations on the relationship between crystallographic orientation and biasing in apatite fission-track measurements. American Mineralogist, 88(5-6), 817-829.

-. (2005) Forward and inverse modeling of low-temperature thermochronometry data. Reviews in mineralogy and geochemistry, 58(1), 275-314.

Ketcham, R.A., Carter, A., Donelick, R.A., Barbarand, J., and Hurford, A.J. (2007) Improved measurement of fission-track annealing in apatite using c-axis projection. American Mineralogist, 92(5-6), 789-798.

Ketcham, R.A., Carter, A., and Hurford, A.J. (2015) Inter-laboratory comparison of fission track confined length and etch figure measurements in apatite. American Mineralogist, 100(7), 1452-1468.

Ketcham, R.A., and Tamer, M.T. (2021) Confined fission-track revelation in apatite: how it works and why it matters. Geochronology, 3(2), 433-464.

Laslett, G., Gleadow, A., and Duddy, I. (1984) The relationship between fission track length and track density in apatite. Nuclear Tracks and Radiation Measurements (1982), 9(1), 29-38.

Laslett, G., Kendall, W., Gleadow, A., and Duddy, I. (1982) Bias in measurement of fission-track length distributions. Nuclear Tracks and Radiation Measurements (1982), 6(2-3), 79-85.

Li, W., Lang, M., Gleadow, A.J., Zdorovets, M.V., and Ewing, R.C. (2012) Thermal annealing of unetched fission tracks in apatite. Earth and Planetary Science Letters, 321, 121-127.

Li, W., Wang, L., Lang, M., Trautmann, C., and Ewing, R.C. (2011) Thermal annealing mechanisms of latent fission tracks: Apatite vs. zircon. Earth and Planetary Science Letters, 302(1-2), 227-235.

Li, W., Wang, L., Sun, K., Lang, M., Trautmann, C., and Ewing, R.C. (2010) Porous fission fragment tracks in fluorapatite. Physical Review B, 82(14), 144109.

Moreira, P., Guedes, S., Iunes, P., and Hadler, J. (2010) Fission track chemical etching kinetic model. Radiation Measurements, 45(2), 157-162.

Paul, T. (1993) Transmission electron microscopy investigation of unetched fission tracks in fluorapatite—physical process of annealing. Nuclear Tracks and Radiation Measurements, 21(4), 507-511.

Paul, T.A., and Fitzgerald, P.G. (1992) Transmission electron microscopic investigation of fission tracks in fluorapatite. American Mineralogist, 77(3-4), 336-344.

Price, P., and Fleischer, R. (1971) Identification of energetic heavy nuclei with solid dielectric track detectors: Applications to astrophysical and planetary studies. Annual Review of Nuclear Science, 21(1), 295-334.

Price, P., Lal, D., Tamhane, A., and Perelygin, V. (1973) Characteristics of tracks of ions of $14 \leqslant Z \leqslant 36$ in common rock silicates. Earth and Planetary Science Letters, 19(3), 377-395.

Price, P., and Walker, R. (1962) Chemical etching of charged-particle tracks in solids. Journal of applied physics, 33(12), 3407-3412.

Ravenhurst, C.E., Roden-Tice, M.K., and Miller, D.S. (2003) Thermal annealing of fission tracks in fluorapatite, chlorapatite, manganoanapatite, and Durango apatite: experimental results. Canadian Journal of Earth Sciences, 40(7), 995-1007.

Rebetez, M., Chambaudet, A., and Mars, M. (1988) Theoretical etching effects on “track in track” and “track in cleavage” length distributions. International Journal of Radiation Applications and Instrumentation. Part D. Nuclear Tracks and Radiation Measurements, 15(1-4), 69-72.

Sobel, E.R., and Seward, D. (2010) Influence of etching conditions on apatite fission-track etch pit diameter. Chemical Geology, 271(1-2), 59-69.

Szenes, G. (1996a) Formation of amorphous latent tracks in mica. Nuclear Instruments and Methods in Physics Research Section B: Beam Interactions with Materials and Atoms, 107(1-4), 146-149.

-. (1996b) Thermal spike model of amorphous track formation in insulators irradiated by swift heavy ions. Nuclear Instruments and Methods in Physics Research Section B: Beam Interactions with Materials and Atoms, 116(1-4), 141-144.

Taborszky, F. (1972) Das problem der Cl-apatite. Lithos, 5(4), 315-324.

Tagami, T., and O’Sullivan, P.B. (2005) Fundamentals of fission-track thermochronology. Reviews in Mineralogy and Geochemistry, 58(1), 19-47.

Tamer, M.T., Chung, L., Ketcham, R.A., and Gleadow, A.J. (2019) Analyst and etching protocol effects on the reproducibility of apatite confined fission-track length measurement, and ambient-temperature annealing at decadal timescales. American Mineralogist: Journal of Earth and Planetary Materials, 104(10), 1421-1435.

Tamer, M.T., and Ketcham, R.A. (2020) The along-track etching structure of fission tracks in apatite: Observations and implications. Chemical Geology, 553, 119809.

Tello, C.A., Palissari, R., Hadler, J.C., Iunes, P.J., Guedes, S., Curvo, E.A., and Paulo, S.R. (2006) Annealing experiments on induced fission tracks in apatite: Measurements of horizontal-confined track lengths and track densities in basal sections and randomly oriented grains. American Mineralogist, 91(2-3), 252-260.

Toulemonde, M., Bouffard, S., and Studer, F. (1994) Swift heavy ions in insulating and conducting oxides: tracks and physical properties. Nuclear Instruments and Methods in Physics Research Section B: Beam Interactions with Materials and Atoms, 91(1-4), 108-123.

Wauschkuhn, B., Jonckheere, R., and Ratschbacher, L. (2015) Xe-and U-tracks in apatite and muscovite near the etching threshold. Nuclear Instruments and Methods in Physics Research Section B: Beam Interactions with Materials and Atoms, 343, 146-152.

Figure captions

Figure 1. Horizontal confined fossil tracks in prism faces of Bamble (BB), Slyudyanka (SY), Brazil (BZ), and Panasqueira (PQ) apatite. The left panel shows the track after the first immersion (t_{I1}) and the right panel after the second immersion (t_{I2}) in 5.5 M HNO_3 at 21 °C. (**a**) BB: t_{I1} = 10 s, t_{I2} = 20 s. (**b**) SY: t_{I1} = 20 s, t_{I2} = 35 s. (**c**) BZ: t_{I1} = 10 s, t_{I2} = 20 s. (**d**) PQ: t_{I1} = 35 s, t_{I2} = 50 s. Measurements: length (l), ***c***-axis angle (ϕ), maximum width (r_0), width (r_1) at distance (s_1) from r_0, and perpendicular distances (d_1 and d_2) between facing sides of the diamond shape, bounded by the fastest etching apatite faces at the intersection with the host track ($\phi \gtrsim 80°$).

Figure 2. (**a**) Transmitted-light microscope image of a horizontal confined track in apatite SY after 20 s immersion. (**b**) Track contour showing the measured dimensions: length (l), ***c***-axis angle (ϕ), and maximum width (r_0); the width (r_1) at a distance (s_1) from (r_0), used for calculating the cone angle (θ) and the track etch rate (v_T), and the apatite etch rate (v_R) perpendicular to the track. (**c**) Principle for calculating θ from r_0 , r_1, and s_1.

Figure 3. Plot of the standard deviations against the means of the confined track length distributions. PQ: Panasqueira; SY: Slyudyanka; BZ Brazil; BB: Bamble; open symbols: lengths measured after the first etch; filled symbols: after second etch. PQ and SY have basement and BZ and BB have volcano-type signatures (Gleadow et al. 1986).

Figure 4. Lengths of confined tracks measured after the second etch plotted against their lengths after the first etch. PQ: Panasqueira; SY: Slyudyanka; BZ Brazil; BB: Bamble; (**a**) PQ; (**b**) SY; (**c**) BZ; (**d**) BB. The dashed line is 1:1 (no length increase); the solid lines are geometric mean regression lines. Anchored (at origin) regression lines parallel to the 1:1 line are not shown but indistinguishable.

Figure 5. Plot of the **a**-axis intercepts vs. **c**-axis intercepts of ellipses fitted to track-length and orientation data. PQ: Panasqueira; SY: Slyudyanka; BZ Brazil; BB: Bamble. Open symbols: data measured after the first etch; filled symbols: after second etch. The RD line illustrates the relationship for induced fission tracks (Donelick et al. 1999).

Figure 6. (**a**) Apatite etch rates of PQ (white), SY (light grey), and BZ (dark grey) plotted against orientation ($\phi' = 90° - \phi$); the solid lines are empirical fits (equation 5). (**b**) Apatite etch rates of BB; the solid line is an empirical fit (equation 9). (**c**) Polar plots comparing the apatite etch rates of PQ (solid line), SY (long-dashed), BZ (medium-dashed), and BB (short-dashed)with the Durango data of Aslanian et al. (2021; DR: Durango apatite; red line). PQ: Panasqueira; SY: Slyudyanka; BZ Brazil; BB: Bamble; DR: Durango data of Aslanian et al. (2021).

Figure 7. Best-fit parameters a and b (equation 5) plotted against $Dpar$; the solid lines are geometric mean regression lines. PQ: Panasqueira; SY: Slyudyanka; BZ: Brazil; the fit further includes the Durango data of Aslanian et al. (2021; DR), which we refitted with equation (5) but not the Bamble data, which were fitted with equation (9).

Figure 8. (**a**) Immersion times (t_I), geometric means (t_{EM}) and standard deviations (σ_{TE}) of the effective etch-time distributions plotted against $Dpar$. PQ: Panasqueira; SY: Slyudyanka; BZ Brazil; BB: Bamble; DR: Durango data of Aslanian et al. (2021). Solid lines are first-order fits proportional to $Dpar^{-1}$. (**b**) Comparison of first-order fits (solid lines) to the means ($25/Dpar$; $t_{EM} \approx ½\ t_I$) and

standard deviations (10/*Dpar;* $\sigma_{TE} \approx ⅕\ t_I$), with best-fits of the form $u + v/Dpar$ (dashed lines), showing good agreement.

Figure 9. (**a**) Geometric means (open) and standard deviations (filled) of the v_T-distributions (track etch rate). (**b**) Geometric means and standard deviations of the v_L-distributions (rate of length increase) plotted against *Dpar*. PQ: Panasqueira; SY: Slyudyanka; BZ: Brazil; BB: Bamble; DR: Durango data of Aslanian et al. (2021). Solid lines are geometric mean regression lines; dashed lines are anchored at the origin.

Figure 10. Mean track lengths plotted against effective etch action (effective etch time × *Dpar*). (**a**) Fossil tracks in Panasqueira (PQ), Slyudyanka (SY), Brazil (BZ), and Bamble (BB). (**b**) Fossil tracks in Durango (DR; Aslanian et al. 2021) and induced track data for different chemical compositions (Carlson et al. 1999; Barbarand et al. 2003). Solid lines are geometric mean regression lines; dotted lines are constrained to the same slope.

Supplement figures

Figure S1. Lengths of fossil confined tracks in the studied apatites measured after the first (t_{I1}) and second immersion (t_{I2}) in 5.5 M HNO_3 at 21 °C, plotted against angle to the ***c***-axis. PQ: Panasqueira ((**a**): t_{I1} = 35 s, (**b**): t_{I2} = 50 s); SY: Slyudyanka ((**c**): t_{I1} = 20 s, (**d**): t_{I2} = 35 s); BZ: Brazil ((**e**): t_{I1} = 10 s, (**f**): t_{I2} = 20 s); BB: Bamble ((**g**): t_{I1} = 10 s, (**h**): t_{I2} = 20 s).

Figure S2. Track length increments (Δl) during the etch time increment (Δt_I) from the first to the second immersion in 5.5 M HNO_3 at 21 °C, plotted against angle to the c-axis (ϕ), and corresponding frequency distributions of Δl in the studied samples. PQ: Panasqueira; SY: Slyudyanka; BZ: Brazil; BB: Bamble. PQ ((**a**) and (**e**); Δt_I = 15 s); SY ((**b**) and (**f**); Δt_I = 15 s); BZ ((**c**) and (**g**); Δt_I = 10 s); BB ((**d**) and (**h**); Δt_I = 10 s); the dashed lines in (e)-(h) represent polynomial fits.

Figure S3. Confined track widths (r_0) after the first immersion in 5.5 M HNO_3 at 21 °C plotted against angle to the ***c***-axis (ϕ), and corresponding angular distributions. PQ: Panasqueira; SY: Slyudyanka; BZ: Brazil; BB: Bamble. PQ ((**a**) and (**e**)); SY ((**b**) and (**f**)); BZ ((**c**) and (**g**)); BB ((**d**) and (**h**)). The lines (1)-(4) in (**a**)-(**d**) are inferred etching and selection biases; (1) theoretical maximum width: $v_R(\phi') \times t_I$; (2) width assuming an average access time t_A to reach the confined track: $v_R(\phi') \times (t_I - t_A)$; (3) threshold width of tracks judged suitable for measurement; (4) minimum width at the host track intersection of tracks etched to both ends (equation 4). The long-dashed lines superimposed on the angular distributions (**e**)-(**h**) show the range of track widths r_0 constrained by criteria (2)-(4) as a function of ϕ.

Figure S4. Effective etch times (t_E) of confined tracks plotted against their angles to the ***c***-axis (ϕ) and corresponding t_E-distributions. PQ: Panasqueira; SY: Slyudyanka; BZ: Brazil; BB: Bamble. PQ ((**a**) and (**e**)); SY ((**b)** and (**f**)); BZ ((**c**) and (**g**)); BB ((**d**) and (**h**)). Open symbols in (**a**)-(**d**): measured using equation 4a (Figure 1a-c); filled symbols: measured using equation 4b (Figure 1d). The dashed lines in (**e**)-(**h**) represent polynomial fits. t_{EM} and σ_{tE}: geometric means and standard deviations of the effective etch-time distributions.

Figure S5. Etch rates (v_T) of confined tracks plotted against their angles to the ***c***-axis (ϕ), and corresponding v_T-distributions. PQ: Panasqueira; SY: Slyudyanka; BZ: Brazil; BB: Bamble. PQ ((**a**) and (**e**)); SY ((**b**) and (**f**)); BZ ((**c**) and (**g**)); BB ((**d**) and (**h**)). The dashed lines in (**e**)-(**h**) represent polynomial fits. v_{TM} and σ_{VT}: geometric means and standard deviations of the track etch-rate distributions.

Figure S6. Rates of length increase (v_L) of confined tracks plotted against their angles to the ***c***-axis (ϕ) and corresponding v_L-distributions. PQ: Panasqueira; SY: Slyudyanka; BZ: Brazil; BB: Bamble. PQ ((**a**) and (**e**)); SY ((**b**) and (**f**)); BZ ((**c**) and (**g**)); BB ((**d**) and (**h**)); the dashed lines in (**e**)-(**h**) represent polynomial fits. v_{LM} and σ_{VL}: means and standard deviations of the distributions of the rate of length increase.

Tables

Table 1. Symbols and their meaning

Symbols	Meaning
r_0	maximum width of confined track
r_1	non-maximum width of confined track
s_1	distance between r_0 and r_1
d_1, d_2	perpendicular distances between facing sides of the diamond shape in confined track
ϕ	angle between the track axis and the apatite ***c***-axis
ϕ'	angle between the apatite etch rate orientation and the apatite ***c***-axis, ($\phi' = 90° - \phi$)
θ	angle between facing straight sides of the confined track
Δr_0	confined track width increase at its intersection with the host track
t_I	immersion time
t_E	effective etch time
t_A	access time ($t_A = t_I - t_E$)
t_{EM}	geometric mean effective etch time
Δt_I	time increment from the first to the second etch
t'_I	etch action with apatite etch rate and immersion time
t'_E	etch action with apatite etch rate and effective etch time
l	measured length of confined track
l_M	mean track length of confined tracks
l_{PM}	mean ***c***-axis-projected length of confined tracks
Δl	length increment of confined track
Δl_M	mean length increment of confined track
l_A	short axis of unconstrained ellipses
l_C	long axis of unconstrained ellipses
v_B	apatite bulk etch rate
v_R	apatite radial etch rate
v_T	fission track etch rate
v_L	rate of length increase
v_{TM}	geometric mean of track etch rates
v_{LM}	geometric mean of rates of length increase
σ_M	standard deviation of mean track length
σ_{PM}	standard deviation of the ***c***-axis-projected lengths
σ_{tE}	standard deviation of the effective etch times
σ_{VT}	standard deviation of the track etch rates
σ_{VL}	standard deviation of the rates of length increase
a, b, c	constants of fitting equation for the hexagonal apatites
I_L	intercepts of regression lines in Figure 4
I_L'	intercepts of constrained regression lines in Figure 4
I_T	intercepts of regression lines in Figure 10
S_L S_L'	slopes of regression lines and constrained regression lines in Figure 4
S_T	slopes of regression lines in Figure 10
r_L	correlation coefficients of regression lines in Figure 4
r_L'	correlation coefficients of constrained regression lines in Figure 4
r_T	correlation coefficients of regression lines in Figure 10

Table 2. Track length data for PQ, SY, BZ, BB and DR apatite (Aslanian et al. 2021). $\boldsymbol{\rho_S}$: track densities of fossil tracks; N_{Track}: number of measured tracks; t_I: immersion time; l_M: mean track length; σ_M: standard deviation of l_M; l_{PM}: mean ***c***-axis-projected length; $\boldsymbol{\sigma_{PM}}$: standard deviation of l_P; l_C and l_A: long and short axes of unconstrained ellipses; Δl_M: length increase between the first and second measurement. Error are 1σ.

Sample	***Dpar*** (μm)	$\boldsymbol{\rho_S}$ (10^6cm^{-2})	$\boldsymbol{t_I}$ (s)	$\boldsymbol{N_{Track}}$	$\boldsymbol{l_M}$ (μm)	$\boldsymbol{\sigma_M}$ (μm)	$\boldsymbol{l_{PM}}$ (μm)	$\boldsymbol{\sigma_{PM}}$ (μm)	$\boldsymbol{l_C}$ (μm)	$\boldsymbol{l_A}$ (m)	$\boldsymbol{\Delta l_M}$ (μm)
PQ	1.60 (1)	1.31 (5)	35	232	12.3 (1)	1.7	13.5 (1)	1.2	12.9 (3)	12.0 (2)	0.46 (2)
			50	221	12.8 (1)	1.7	13.8 (1)	1.3	13.3 (3)	12.5 (2)	
DR	1.85 (2)	0.18 (0)	30	205	14.2 (1)	1.0	14.9 (1)	0.7	15.0 (2)	13.8 (1)	0.67 (2)
			45	205	14.8(1)	1.0	15.4 (1)	0.7	15.7 (1)	14.4 (1)	
SY	2.44 (1)	4.15 (19)	20	226	13.1 (1)	1.7	14.0 (1)	1.3	14.1 (3)	12.8 (2)	0.80 (3)
			35	222	13.9 (1)	1.8	14.6 (1)	1.4	14.8 (3)	13.5 (2)	
BZ	3.92 (2)	11.1 (5)	10	209	15.6 (1)	0.8	16.0 (1)	0.6	15.7 (2)	15.6 (1)	0.97 (2)
			20	208	16.6 (1)	0.8	16.7 (1)	0.6	16.6 (2)	16.6 (1)	
BB	4.60 (4)	0.63 (3)	10	199	13.4 (1)	1.1	14.2 (1)	0.8	14.0 (2)	12.9 (2)	1.13 (4)
			20	199	14.5 (1)	1.0	15.1 (1)	0.8	15.3 (2)	13.9 (1)	

Table 3. Intercepts (I), slopes (S), and correlation coefficients (r) of geometric mean regression lines to the track lengths measured after the second immersion plotted against the values measured after the first immersion (Figure 4; I_L, S_L, r_L). Intercepts (I_L') and correlation coefficients (r_L') of regression lines to the same data, constrained to have slopes S_L' =1. Intercepts, slopes, and correlation coefficients of geometric mean regression lines to plots of the interpolated mean track lengths against the effective etch action t_E' (Figure 10; I_T, S_T, r_T). DR data from Aslanian et al. (2021).

Sample	***Dpar*** (μm)	$\boldsymbol{I_L}$ (μm)	$\boldsymbol{S_L}$ (-)	$\boldsymbol{r_L}$ (-)	$\boldsymbol{I_L'}$ (μm)	$\boldsymbol{r_L'}$ (-)	$\boldsymbol{I_T}$ (μm)	$\boldsymbol{S_T}$ (min^{-1})	$\boldsymbol{r_T}$ (min^{-1})
PQ	1.60 (1)	0.28	1.01	0.985	0.458	0.985	11.88	1.13	0.989
SY	2.44 (1)	0.31	1.04	0.963	0.927	0.963	12.55	1.11	0.970
BZ	3.92 (2)	0.15	1.05	0.952	0.973	0.952	15.08	1.34	0.987
BB	4.60 (4)	1.79	0.95	0.865	1.135	0.844	12.75	1.56	0.976
DR	1.85 (2)	1.00	0.98	0.947	0.688	0.944	13.30	1.64	0.971

Table 4. Parameters of the $v_R(\phi')$-equation (4) fitted to the data for PQ, SY, and BZ, and DR of Aslanian et al. (2021) (**Figure 6**).

Sample	***Dpar*** (μm)	***a*** (μm/(min.°))	***b*** (1/°)	***c*** (μm.min^{-1})
PQ	1.60 (1)	0.31 (1)	-0.049 (1)	0.06 (8)
DR	1.85 (2)	0.36 (1)	-0.051 (1)	0.26 (8)
SY	2.44 (1)	0.42 (1)	-0.051 (1)	0.10 (8)
BZ	3.92 (2)	0.64 (1)	-0.054 (1)	0.15 (8)

Table 5. Geometric means and standard deviations of the effective etch times, track etch rates, and rates of length increase of the studied samples, and their correlations with fitted power functions (t_{EM} and σ_{tE}) and regression lines (v_{TM}, σ_{VT}, v_{LM}, and σ_{VL}).

Sample	***Dpar*** (μm)	$\boldsymbol{t_I}$ (s)	$\boldsymbol{t_{EM}}$ (s)	$\boldsymbol{\sigma_{tE}}$(s)	$\boldsymbol{v_{TM}}$ (μm.min^{-1})	$\boldsymbol{\sigma_{VT}}$ (μm.min^{-1})	$\boldsymbol{v_{LM}}$ (μm.min^{-1})	$\boldsymbol{\sigma_{VL}}$ (μm.min^{-1})
PQ	1.60 (1)	35	15.8 (5)	7.2	103 (5)	66	0.76 (4)	0.51
SY	2.44 (1)	20	12.1 (2)	3.2	95 (3)	37	1.41 (6)	0.79
BZ	3.92 (2)	10	5.69 (1)	1.6	197 (5)	70	2.82 (6)	0.76
BB	4.60 (4)	10	5.24 (1)	1.9	192 (6)	78	3.08 (11)	1.52
DR	1.85 (2)	30	17.9 (7)	7.2	78 (2)	24	1.17 (6)	0.64
$r(Dpar)$		0.99	0.98	0.96	0.93	0.67	0.99	0.84

Figure 1

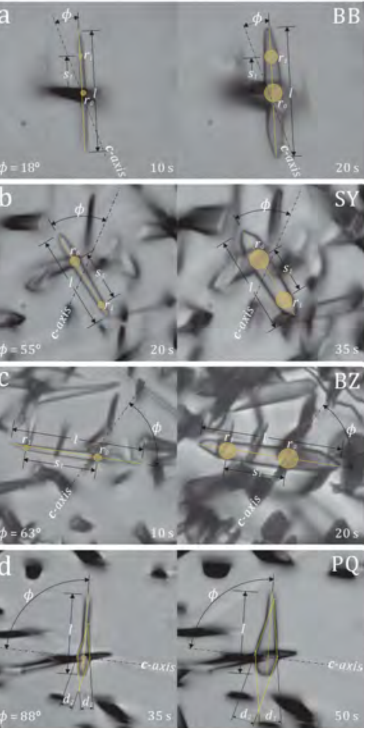
a
BB
ϕ = 18°
10 s
20 s
c-axis
b
SY
ϕ = 55°
20 s
35 s
c-axis
c
BZ
ϕ = 63°
10 s
20 s
c-axis
d
PQ
ϕ = 88°
35 s
50 s
c-axis

igure 2

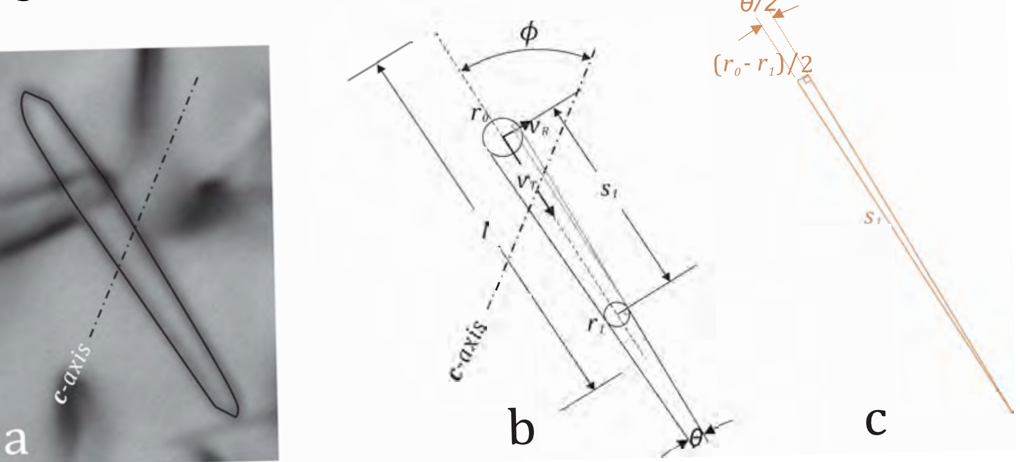

Figure 3

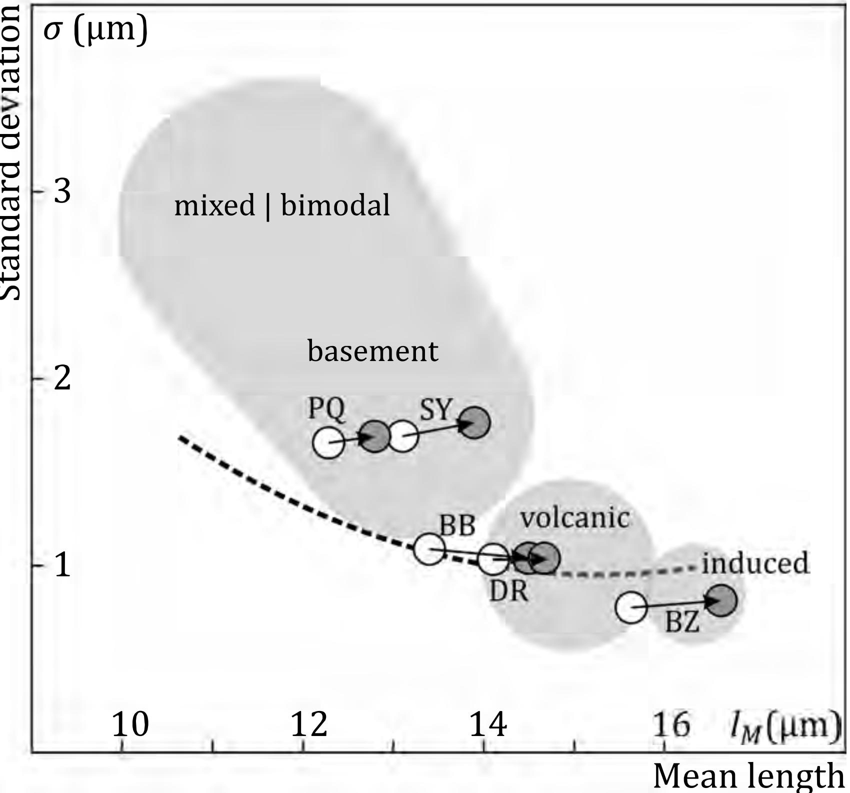

Standard deviation
σ (μm)
3
2
1
mixed | bimodal
basement
PQ
SY
BB
volcanic
DR
induced
BZ
10
12
14
16
l_M(μm)
Mean length

Figure 4

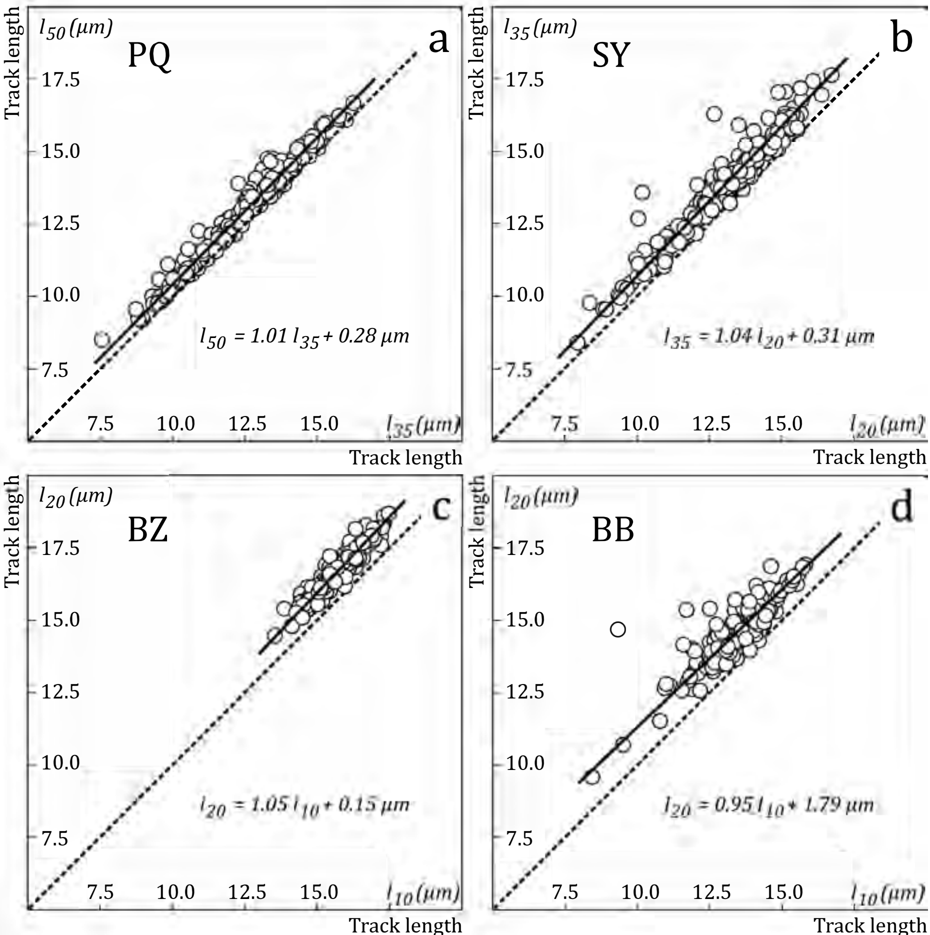

l_{50} (μm)
PQ
a
17.5
15.0
12.5
10.0
7.5
7.5
10.0
12.5
15.0
l_{35} (μm)
l_{50} = 1.01 l_{35} + 0.28 μm
Track length
Track length
l_{35} (μm)
SY
b
l_{35} = 1.04 l_{20} + 0.31 μm
l_{20} (μm)
Track length
Track length
l_{20} (μm)
BZ
c
l_{20} = 1.05 l_{10} + 0.15 μm
l_{10} (μm)
Track length
Track length
l_{20} (μm)
BB
d
l_{20} = 0.95 l_{10} + 1.79 μm
l_{10} (μm)
Track length
Track length

Figure 5

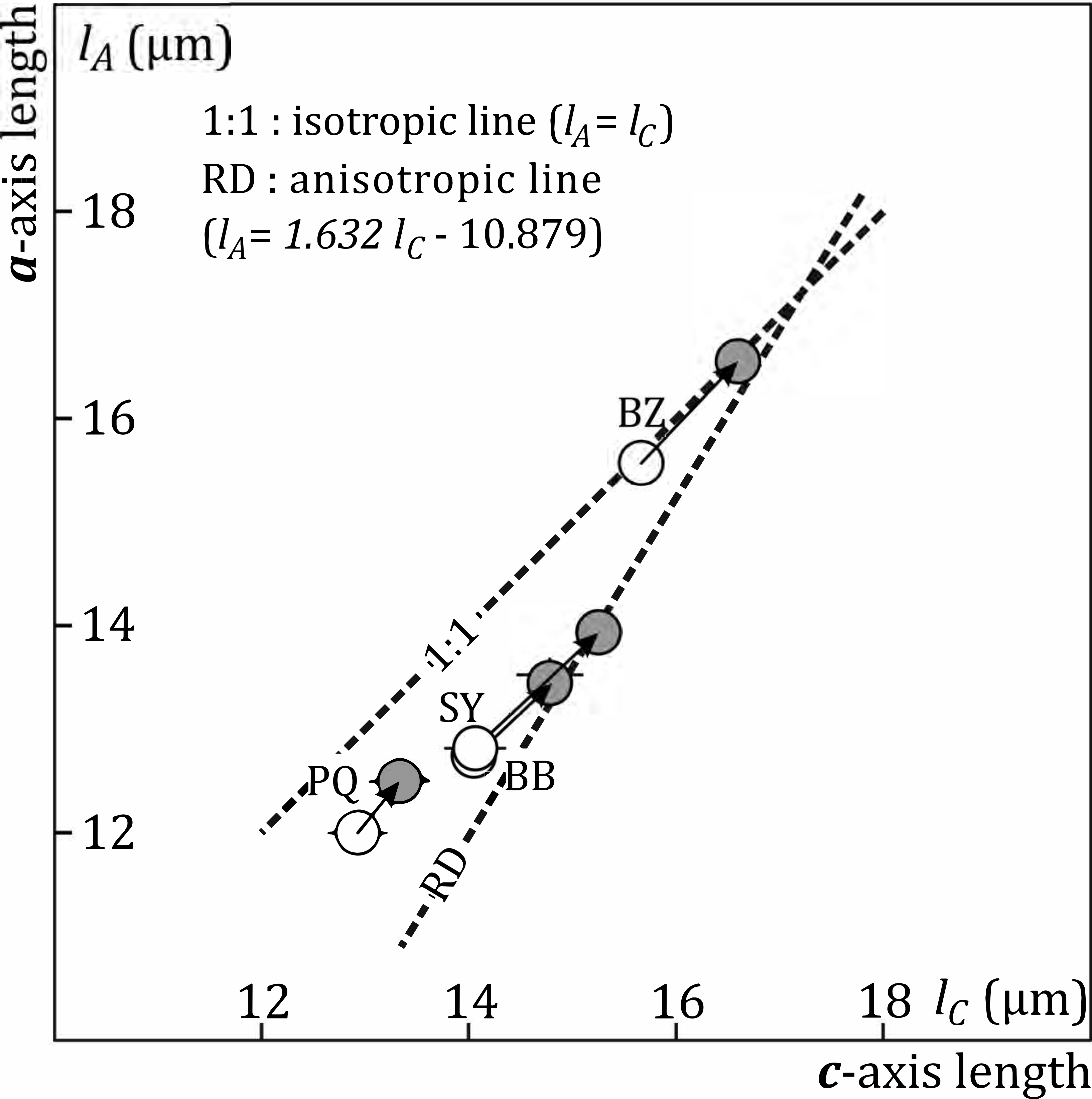

a-axis length
l_A (μm)
1:1 : isotropic line ($l_A = l_C$)
RD : anisotropic line
($l_A = 1.632\ l_C - 10.879$)
18
16
14
12
BZ
SY
BB
PQ
1:1
RD
12
14
16
18
l_C (μm)
c-axis length

Figure 6

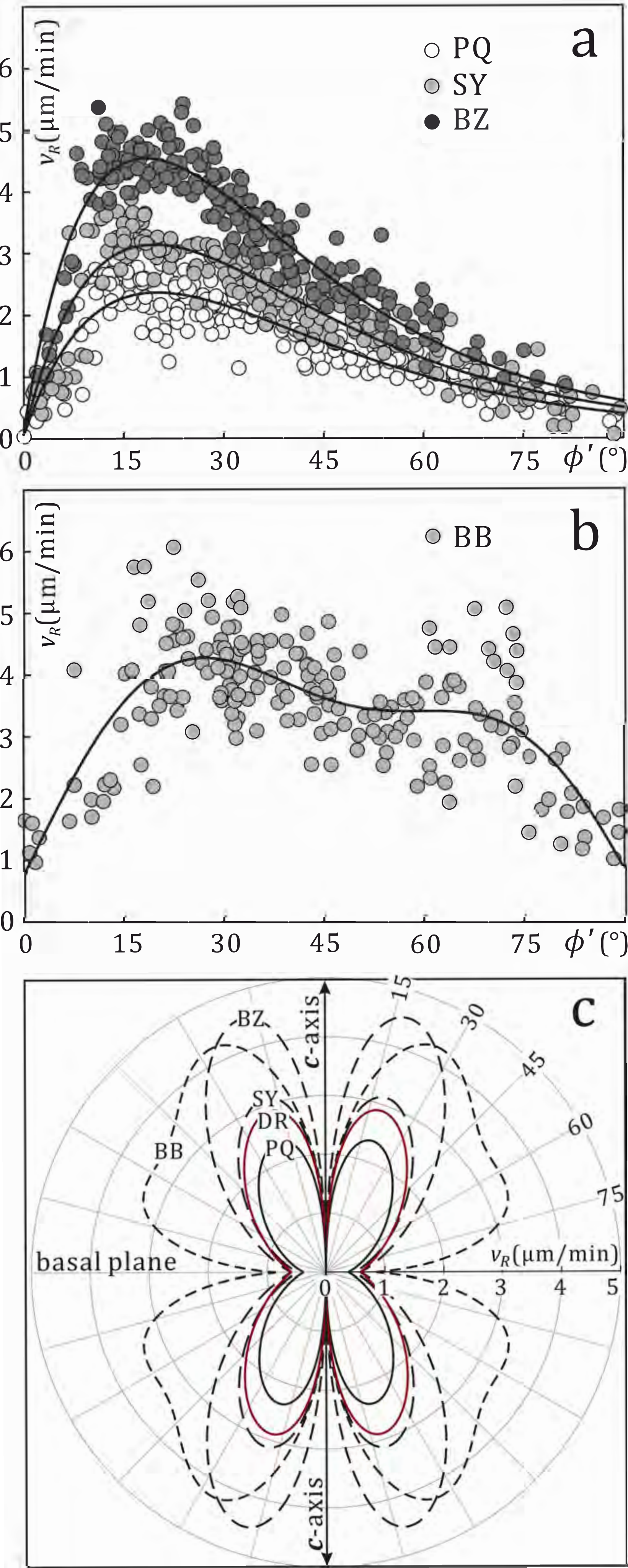

a
PQ
SY
BZ
v_R(μm/min)
ϕ'(°)
b
BB
v_R(μm/min)
ϕ'(°)
c
c-axis
BZ
SY
DR
PQ
BB
basal plane
v_R(μm/min)
15
30
45
60
75

Figure 7

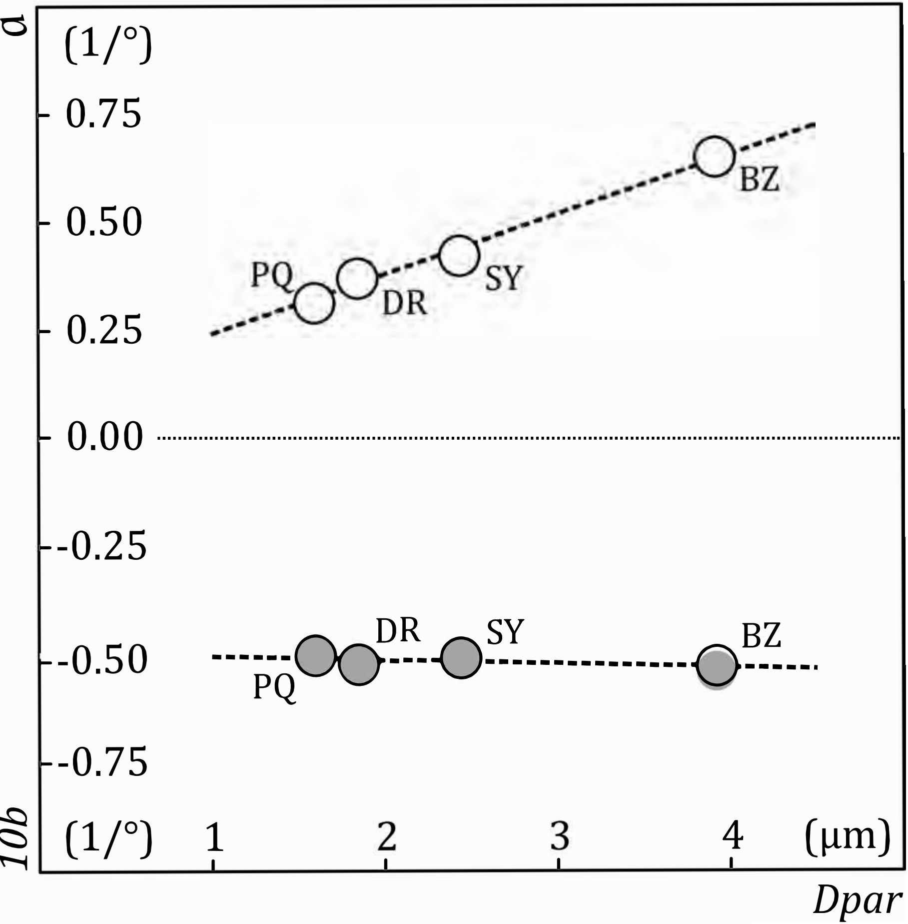

a
(1/°)
0.75
0.50
0.25
0.00
-0.25
-0.50
-0.75
10b
(1/°)
PQ
DR
SY
BZ
PQ
DR
SY
BZ
1
2
3
4
(µm)
Dpar

Figure 8

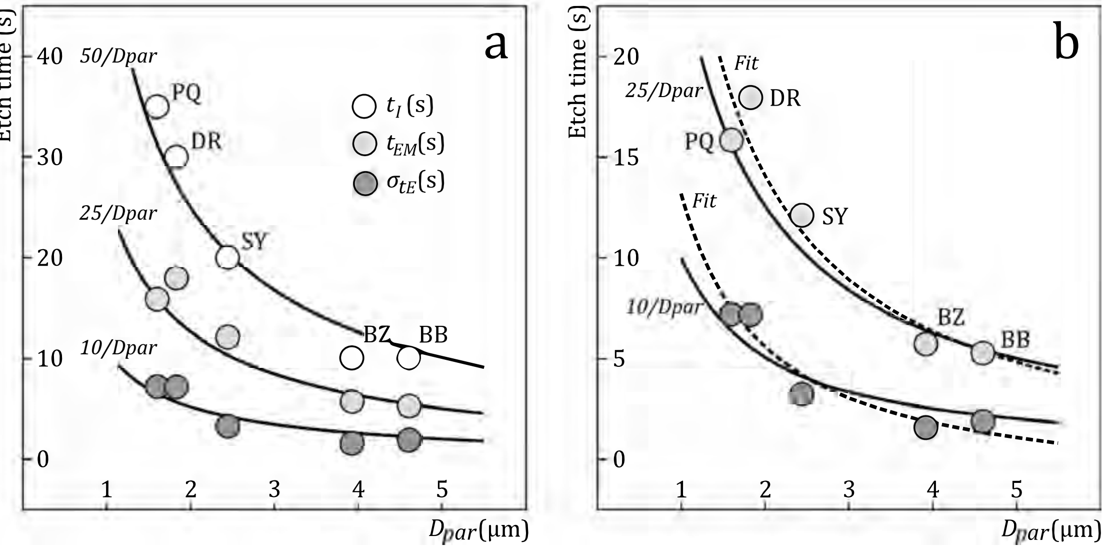

a
Etch time (s)
40
30
20
10
0
50/Dpar
25/Dpar
10/Dpar
PQ
DR
SY
BZ
BB
t_I (s)
t_{EM}(s)
σ_{tE}(s)
1
2
3
4
5
D_{par}(μm)
b
Etch time (s)
20
15
10
5
0
Fit
25/Dpar
DR
PQ
SY
Fit
10/Dpar
BZ
BB
1
2
3
4
5
D_{par}(μm)

Figure 9

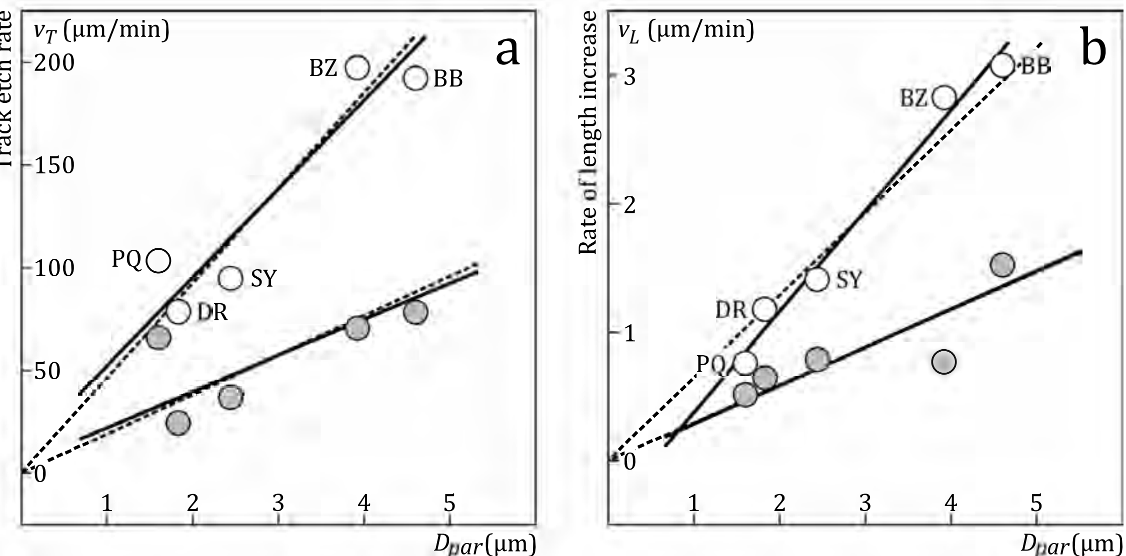

Track etch rate
vT (µm/min)
a
200
150
100
50
0
BZ
BB
PQ
SY
DR
1
2
3
4
5
Dpar(µm)
Rate of length increase
vL (µm/min)
b
3
2
1
0
BZ
BB
SY
DR
PQ
1
2
3
4
5
Dpar(µm)

Figure 10

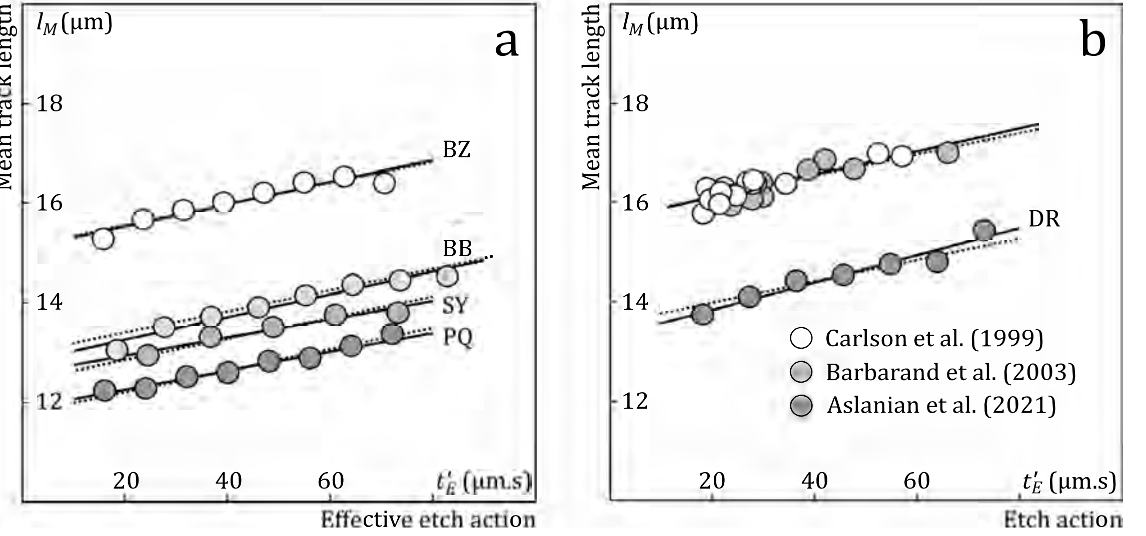

Mean track length
l_M (μm)
a
18
16
14
12
BZ
BB
SY
PQ
20
40
60
t'_E (μm.s)
Effective etch action
Mean track length
l_M (μm)
b
18
16
14
12
DR
Carlson et al. (1999)
Barbarand et al. (2003)
Aslanian et al. (2021)
20
40
60
t'_E (μm.s)
Etch action